



ELSEVIER

Contents lists available at ScienceDirect

Applied Clay Science

journal homepage: www.elsevier.com/locate/clay

Research Paper

Imogolite in water: Simulating the effects of nanotube curvature on structure and dynamics



Rafael I. González^{a,b,*}, Javier Rojas-Nunez^{c,b}, Felipe J. Valencia^{d,b}, Francisco Munoz^{e,b}, Samuel E. Baltazar^{c,b}, Sebastián Allende^{c,b}, José Rogan^{e,b}, Juan Alejandro Valdivia^{e,b}, Miguel Kiwi^{e,b}, Ricardo Ramírez^{f,b}, Jeffery A. Greathouse^g

^a Centro de Nanotecnología Aplicada, Universidad Mayor, Santiago, Chile

^b Centro para el Desarrollo de la Nanociencia y la Nanotecnología, CEDENNA, Avda. Ecuador 3493, Santiago 9170124, Chile

^c Departamento de Física, Universidad de Santiago de Chile, Av. Ecuador 3493, Santiago 9170124, Chile

^d DAiTA Lab, Facultad de Estudios Interdisciplinarios, Universidad Mayor, Santiago, Chile

^e Departamento de Física, Facultad de Ciencias, Universidad de Chile, Casilla 653, Santiago 7800024, Chile

^f Instituto de Física, Pontificia Universidad Católica de Chile, Av. Vicuña Mackenna 4860, Macul, Santiago, Chile

^g Geochemistry Department, Sandia National Laboratories, Albuquerque, NM 87111, USA

ARTICLE INFO

Keywords:

Imogolite

Nanotubes

ClayFF

Molecular dynamics simulations

ABSTRACT

Imogolite is a fascinating inorganic nanotube that is found in nature or synthesized in a laboratory. The synthesis process is carried out in liquid media, and leads to the formation of almost monodisperse diameter nanotubes. Here we investigate, employing classical molecular dynamics simulations, the interaction of water and imogolite for nanotubes of several radii. We established that water penetrates the pores of $N = 9$ and larger nanotubes, and adopts a coaxial arrangement in it. Also, while water molecules can diffuse along the center of the nanotube, the molecules next to the inner imogolite walls have very low mobility. At the outer nanotube wall, an increase of water density is observed, this effect extends up to 1 nm, beyond which water properties are bulk-like. Both phenomena are affected by the imogolite curvature.

1. Introduction

Imogolite is a naturally occurring aluminosilicate clay mineral nanotube (NT) of variable diameter, which is much smaller than the NT length. It is believed that the NT interior is accessible to water and aqueous species, making imogolite a potentially useful material for the adsorption or separation of pollutants in soils and liquids. For example, imogolite has been shown to have five times larger retention capacity for arsenic than commercially available materials (Gustafsson, 2001; Arancibia-Miranda et al., 2014). It could also be used for the containment of oil spills, as a thickening agent of lotions and creams, and for drug delivery (Veerabadrán et al., 2007). Other potential applications for imogolite include polymer support for catalysts (Imamura et al., 1993; Liz-Marzan and Philipse, 1994; Imamura et al., 1996; Park et al., 2007; Arancibia-Miranda et al., 2015), as molecular sieves (Denaix et al., 1999; Wilson et al., 2002; Zanzoterra et al., 2012) and gas sorbents (Kang et al., 2012, 2014), or as a component of nanowires and organic-inorganic nanohybrids (Yamamoto et al., 2007; Kuc and Heine, 2009; Yah et al., 2011; Kang et al., 2011; Bottero et al., 2011; Ma et al.,

2012; Geraldo et al., 2012; Thomas et al., 2012; Ramírez et al., 2015).

Natural imogolite is found in Japan (Yoshinaga and Aomine, 1962) and Chile in aged volcanic ashes (Besoain, 1969; Besoain et al., 2000). The chemical composition of single-walled imogolite is $[(\text{OH})_3\text{Al}_2\text{O}_3\text{SiOH}]_{2N}$, angularly repeated N times, as illustrated in Fig. 1. This structure, of significant relevance in the study of imogolite, was put forward by Cradwick et al. (1972). Shortly thereafter, Farmer et al. (1977) published a protocol for its synthesis.

Controlling the morphology of synthetic nanoparticles remains the focus of significant research efforts. Fortunately, for imogolite, the effective control of particle size is possible within a narrow range of approximately 2 nm in diameter, while its length is less restricted with 100 nm as a representative size (Mukherjee et al., 2005; Yucelen et al., 2012b). Based on experimental evidence, and independent of several reported synthesis methods, only a narrow range of NT diameters has been reported (Farmer et al., 1977; Barret et al., 1991; Bursill et al., 2000; Mukherjee et al., 2005; Levard et al., 2009). This narrow range has been confirmed by theoretical calculations of strain energies for different diameters (Guimaraes et al., 2007; Alvarez-Ramírez, 2007;

* Corresponding author at: Centro de Nanotecnología Aplicada, Universidad Mayor, Santiago, Chile.

E-mail address: rafael.gonzalez@umayor.cl (R.I. González).

<https://doi.org/10.1016/j.clay.2020.105582>

Received 15 November 2019; Received in revised form 12 February 2020; Accepted 19 March 2020

Available online 30 April 2020

0169-1317/ © 2020 Elsevier B.V. All rights reserved.

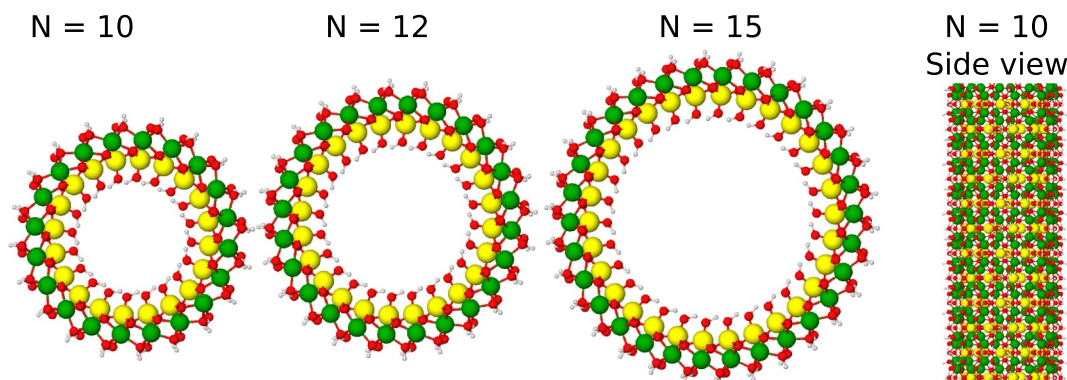


Fig. 1. Imogolite structure from an axial and lateral point of view. The cases of $N = 10$, 12, and 15 are shown from an axial point of view, and $N = 10$ from a lateral view. The basic imogolite unit $[(\text{OH})_3 \text{Al}_2\text{O}_3\text{SiOH}]_2$, ordered from the outer to the inner wall of the NT. H: light gray, O: red, Si: yellow and Al: green. (For interpretation of the references to colour in this figure legend, the reader is referred to the web version of this article.)

González et al., 2014). Moreover, we reported a minimum of the strain energy for a value of $N = 10$ repetitions of the molecular unit (González et al., 2014), a value that is close to natural imogolite, and that also agrees with several theoretical works (Guimaraes et al., 2007; Alvarez-Ramírez, 2007). Experimentally, Yucelen systematically studied the growth of imogolite NTs (Yucelen, 2012; Yucelen et al., 2011, 2012b, 2012a, 2013). He also confirmed the existence of proto-imogolite, characterized the precursor nanoparticles for the NT formation (Yucelen et al., 2011; González et al., 2018), and showed that the NT diameter can be modified in the range 2.2 – 2.8 nm, by changing the anion used during synthesis (Yucelen et al., 2012b). Similarly, Arancibia-Miranda et al. (2017) showed the possibility of fine control of the diameter of imogolite by varying the precursors.

Many of the potential applications of imogolite require that the interaction of these NTs with fluids be studied at the molecular level (Creton et al., 2008a,b; Konduri et al., 2008; Zang et al., 2009; Liou et al., 2017; Scalfi et al., 2018; Lisuzzo et al., 2018). The retention and transport of fluids and dissolved species critically depends on the interfacial properties of these fluids at both the interior and exterior surfaces of imogolite NTs. Here we present our molecular simulation results for the structure and dynamics of water near imogolite NT surfaces, using the ClayFF potential (Cygan et al., 2004). We study the adsorption and dynamics of water in NT interiors for diameters consistent with synthesized samples ($N = 8$ –15), and we also investigate the structure and dynamics of NT exteriors immersed in water. The fundamental insight gained from these simulations will contribute to the development of these materials for a range of additional applications.

Our work differs from previous simulations in several important ways, in particular from the work of Scalfi et al. (2018). We use angle bending terms for surface AlOH and SiOH interactions that have been specifically derived for compatibility with ClayFF (Pouvreau et al., 2017). Further, these angle bending terms accurately reproduce the structure and vibrational properties of hydroxylated mineral surfaces, as predicted by DFT. Also, we used the SPC/Fw (Wu et al., 2006) water model that yields values closer to experiment for the diffusion and viscosity coefficients than other commonly used models (Raabe and Sados, 2012). We compare water structure and dynamics for a range of NT diameters to determine the effects of the imogolite structure on water properties. Finally, we study the structure of water inside the NTs as well as on the external surface. The external surface is convex and represents a unique geometry to compare water interfacial properties with the corresponding planar surfaces (Pouvreau et al., 2017).

2. Methods

2.1. Molecular dynamics simulations

All molecular dynamics simulations and geometry optimizations were performed with the LAMMPS code (Large-scale Atomic/Molecular Massively Parallel Simulator) (Plimpton, 1995) accelerated for GPU capabilities (Brown et al., 2011). For atomic interactions we used the ClayFF (Cygan et al., 2004) potential which has shown to be suitable for modeling this type of NT (Konduri et al., 2006, 2007, 2008; Zang et al., 2009, 2010; González et al., 2014, 2016). ClayFF incorporates partial charges associated with each atom, Lennard-Jones interactions, harmonic bonds, and harmonic angular terms. Its original functional form for non-bonded interactions is as follows

$$E = \sum_{i < j} \frac{1}{4\pi\epsilon_0} \frac{q_i q_j}{r_{ij}} + \epsilon_{ij} \left[\left(\frac{\sigma_{ij}}{r_{ij}} \right)^{12} - 2 \left(\frac{\sigma_{ij}}{r_{ij}} \right)^6 \right],$$

where $\sigma_{ij} = 1/2(\sigma_i + \sigma_j)$ and $\epsilon_{ij} = (\epsilon_i \epsilon_j)^{1/2}$. Further details can be found in the original publication (Cygan et al., 2004) and the extension proposed by Konduri et al. (2007). Some improvements to the original ClayFF parameters were used here such as the replacement of the harmonic term for O–H interactions by a Morse potential (Greathouse et al., 2009), and the use of harmonic angle terms for Al–O–H and Si–O–H (ClayFF-MOH) (Pouvreau et al., 2017). Finally, for water interactions, we used the SPC/Fw force field (Wu et al., 2006). For this model, based on flexible SPC (Berendsen et al., 1981), the bonding terms were adjusted to obtain a better agreement with the experimental diffusion data. The details of the potential used and its parameters are included in the Supplementary Materials, along with example input files.

We used a simulation box of $10 \times 10 \times 5$ nm with 3D periodic boundary conditions. The NT is aligned along the z -axis, and molecules cannot be interchanged between the NT inner pore and its surrounding regions. For the long-range interactions the particle-particle particle-mesh (PPPM) method was used (Hockney and Eastwood, 1988). The rRESPA multi-timescale integrator, with inner-loop and outer-loop time steps of 0.5 and 1 fs was also used (Tuckerman et al., 1992).

Imogolite nanotubes were simulated with compositions of $N = 8$ –15. Following the experimental and theoretical linear relations of theoretical N values and experimental estimations of diameters presented by Yucelen et al. (2012b), these are internal and external NT diameters roughly of 0.6–1.0 nm and 1.75–2.8 nm, respectively. To determine the number of water molecules inside the NT pore, we used grand canonical

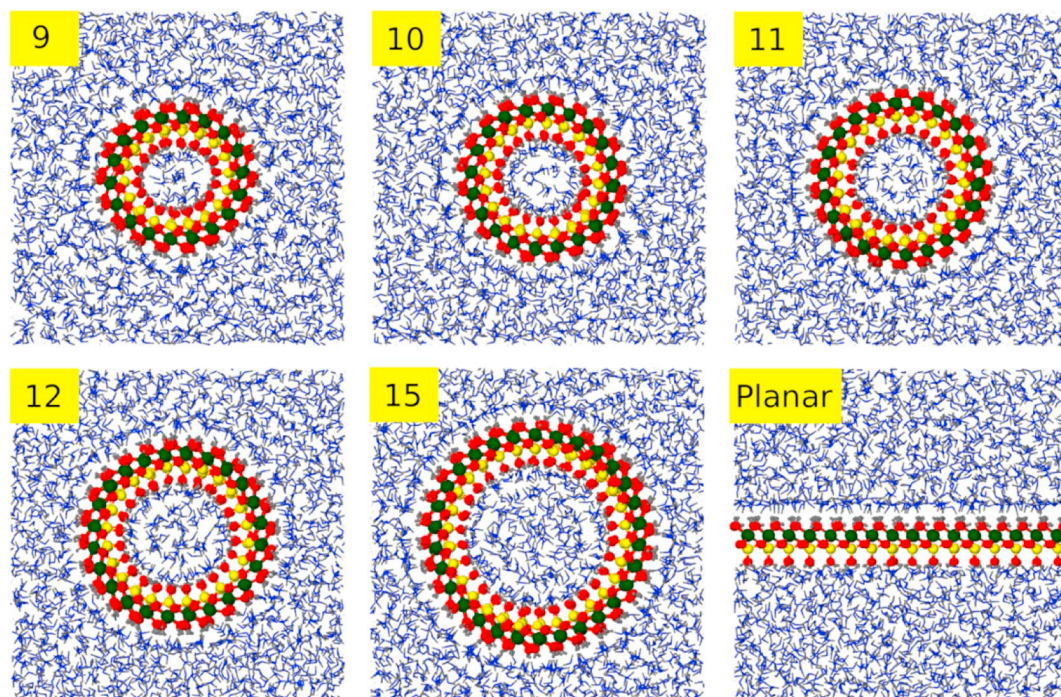


Fig. 2. Water in the inner pore from MD simulations. The number of repetitions N is indicated at each panel. The water box is relaxed with NPT simulations at a pressure 1 atm applied in the xy directions. The box length along the z -axis is maintained fixed.

Monte Carlo simulations (GCMC) (Teich-McGoldrick et al., 2015) as described below. Once we filled the inner pore of imogolite, we added water molecules to the surrounding box. To do so, we randomly inserted one water molecule at each step, making sure not to add any new water molecules at a distance smaller than 1.7 Å to any atom in the box. Next, the box was equilibrated at 300 K using the NVT method with a Nosé-Hoover thermostat, followed by an NPT simulation, keeping the z -axis fixed and relaxing in the xy plane under a pressure of 1 atm for 1 ns. Finally, after the constant pressure simulation was run, an additional 3-ns NVT simulation was performed, using the average box length obtained from the NPT simulation. To avoid any NT drift, we pinned three inner wall oxygen imogolite atoms. To improve statistics, for each value of N , five independent simulations were made; that is, each of these simulations was initiated with different random velocity distributions. Snapshots of the configurations obtained by this procedure are shown in Fig. 2.

For the graphics and post-processing of the results, we used the Open Visualization Tool code OVITO (Stukowski, 2010) and pizza.py tools included with the LAMMPS code.

2.2. Grand canonical Monte Carlo simulations

Water adsorption inside $N = 8$ –15 imogolite NTs at 300 K and 100% relative humidity (RH) were obtained from GCMC simulations using the Towhee code (Martin, 2013) in the grand canonical ensemble (μ VT), where μ is the water chemical potential. Supercells were created by $1 \times 1 \times 3$ repetitions of each imogolite unit cell (UC) model. For computational efficiency, imogolite atoms (except inner hydroxyl H atoms) remained fixed at their coordinates during the subsequent GCMC simulations. Water molecules were modeled as rigid bodies using the SPC/E model (Berendsen et al., 1987) for computational efficiency. A water chemical potential of ($-49.0 \text{ kJ} \cdot \text{mol}^{-1}$) was used, which corresponds to 100% RH based on the saturation chemical potential of SPC/E water (Botan et al., 2011). Short-range interactions were truncated at 10 Å, and long-range electrostatics were computed using Ewald summation with an accuracy of 1.0×10^{-4} . Water GCMC movements were made according to the following probabilities: 40%

configurational-bias insertion or deletion, 15% intrabox configurational-bias molecule transfer, 15% molecule regrowth, 15% center-of-mass translation, and 15% rotation about the center of mass. Up to five successive stages of 1×10^8 steps each were performed to verify that the water density reached equilibrium. Example Towhee input files are included as Supplementary materials.

3. Results and discussion

As far as we know, this work is the first time that the harmonic angular coefficients, recently developed for ClayFF-MOH (Pouvreau et al., 2017), were used to simulate imogolite nanotubes. In 2018, Scalfi et al. (2018) used angular harmonic terms presented as optional (ClayFF-orig) in the original ClayFF paper (Cygan et al., 2004) and compared them for the case of $N = 12$ with DFT calculations. The DFT methods used in that study employed a solid-adapted exchange-correlation functional PBEsol with basis sets of double-zeta valence polarized (Davidson and Feller, 1986; Csonka et al., 2009). In Fig. 3, we show the comparison of Gaussian normalized angular distribution that we obtained for Al-O-H and Si-O-H angles in the case of $N = 12$ at 300 K against Scalfi et al. results. As they discussed, angular terms are an essential ingredient to consider because of the proper comparison with their DFT calculations on both surfaces of the nanotube. In our opinion, the ClayFF-MOH terms yield a width of the angular distribution closer to that of the DFT calculations (σ values in Fig. 3), but the optional terms of ClayFF-orig have a maximum closer to DFT calculations for Al-O-H term and quite similar for the Si-O-H term. The new angle bending terms included in Clayff-MOH were carefully derived by comparing both structural and vibrational properties of representative configurations calculated with DFT. The optional angle bending terms in ClayFF-orig were included in an *ad hoc* manner without such validation. Although neither angle bending approach yields perfect agreement with DFT for the imogolite structures, we chose to use Clayff-MOH parameters in order to maintain consistency with more recent (and future) studies that also use Clayff-MOH.

As mentioned in the previous section, GCMC simulations were performed for imogolite NTs as a function of their diameter, *i.e.*, for

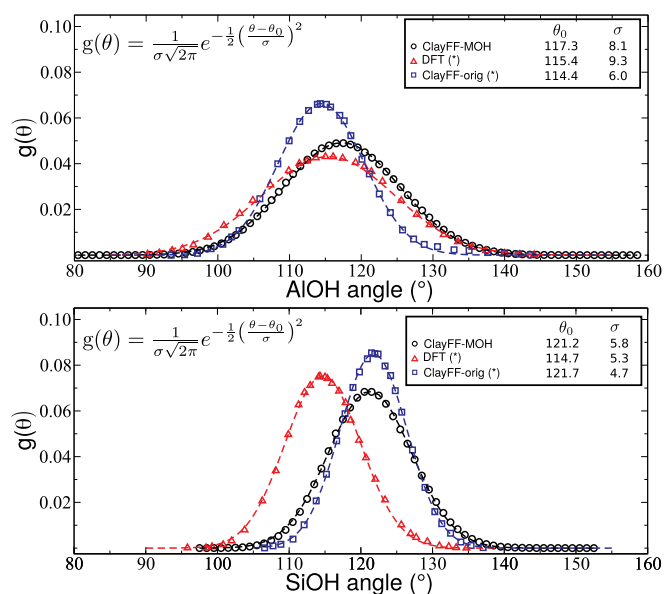


Fig. 3. Angle normalized Gaussian distributions for imogolite $N = 12$ at 300 K. (*) DFT and ClayFF-orig denote cases from Scaffi et al. (2018). ClayFF-orig are results computed using the optional angular term published with ClayFF (Cygan et al., 2004).

Table 1

Results of the GCMC calculations. Imogolite size N , the average number of water molecules Nw (normalized by unit cell), ^athe effective vdW diameter r , and the mean water density ρ .

N	$Nw/u.c.$	r (Å)	ρ (g/cm ³)
8	0.02	4.50	0.004
9	9.39	6.01	1.185
10	16.09	7.51	1.303
11	23.34	8.94	1.319
12	29.54	10.48	1.213
13	38.08	11.89	1.214
14	49.22	13.48	1.226
15	58.70	15.03	1.173

^a Accessible volumes were calculated using the HOLE code (Smart et al., 1996).

$8 \leq N \leq 15$. For $N = 8$ the H₂O molecules cannot penetrate inside the pore. In Table 1, we show the water loading inside the pore, obtained from the GCMC simulations, the effective diameters computed with the HOLE code (Smart et al., 1996), and the mean water density. From this table, we see that the value of the density of water in the pore is, roughly, between 15 and 30% higher than for bulk water. The highest density is for $N = 10-11$ and tends to decrease as the diameter of the nanotube grows.

In Fig. 2, we show final snapshots. In these snapshots, we observe that water inside the pore has a well defined structure. For example, for $N = 10-12$, we can define a coaxial structure, with a water region close to the inner imogolite wall and some water at the NT center. This coaxial conformation is observed even in the largest nanotube ($N = 15$). As mentioned previously, the $N = 9$ case corresponds to the smallest pore diameter in which water was favorably inserted inside the nanotube. Of all the nanotubes shown, it is the only case where water does not occupy the entire inner surface of the pore instantaneously. A well defined layer of adsorbed water is also seen at the external surfaces. The planar case, which does not exist experimentally, but is presented as an extreme case of a very large radius nanotube, has layers of water adsorbed on both surfaces.

At the inner and outer walls of imogolite, water forms ordered layers (Fig. 2). This order can be better quantified from cylindrical

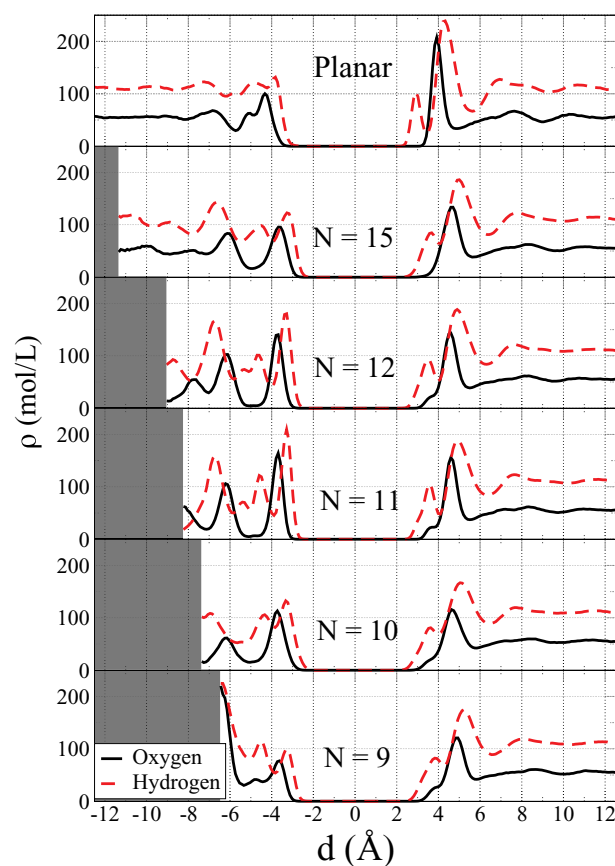


Fig. 4. Cylindrical density profiles of water inside ($d < -2$ Å) and outside ($d > 2$ Å) imogolite nanotubes. Note that $d = 0$ corresponds to the middle of the aluminosilicate wall.

water density profiles in Fig. 4. These profiles were obtained by binning the position of water O and H atoms during the production stages. They are consistent with the previous MD simulations of water in the $N = 12$ NT (Scaffi et al., 2018). The prominent O peak at the inner wall is always accompanied by H peaks on either side of the O peak, suggesting the formation of hydrogen bonds (H-bonds) between the water molecules and surface silanols at the inner wall. Even though this arrangement is dominant, a few water molecules are oriented with both H atoms pointing either toward the surface or away from the surface. This is most noticeable for $N = 11$ and $N = 12$. The variation in the intensity of the first O peak at the inner wall highlights the important effects of surface curvature and pore diameter on water structure. As the pore diameter increases from $N = 9$, the first O peak increases to a maximum value of ≈ 150 mol/L for $N = 11$ and $N = 12$, before decreasing to 100 mol/L for $N = 15$ and the planar model. The maximum values of the first H peak show the same trend as the O peak, while the intensity of the second H peak is approximately 100 mol/L for all models.

Water structure in the inner regions varies considerably beyond the first water layer. The second O peak at $d = -6$ Å (measured from the middle of the imogolite wall) is quite prominent in the smaller NTs. The intensity of this peak diminishes for the $N = 15$ NT and planar models due to the presence of a bulk-like water region farther from the wall at $d = -8$ Å.

At the outer wall, the water structure is consistent for all NT models and the planar model, in terms of the relative peak heights of H atoms to O atoms in the first water layer. The variation in peak heights of the first water layer with pore size is due to differences in the curvature of the gibbsite-like surface. This curvature results in broader water O and H peaks, and even a slight shoulder in the O peak for $N = 9$ through $N = 12$ NTs. Contrary to the interface with the inner wall, at the

interface between water and the outer wall, the larger concentration of H occurs in the second layer of water. This feature indicates that these water molecules donate more H-bonds to the second water layer than to the surface aluminols. This first layer of water molecules is still highly ordered, but there is significantly more water exchange between the first two layers at the outer walls than at the inner walls. This can be seen from the minima between the first and second O peaks in Fig. 4, and also from the snapshots in Fig. 2.

From the previous analysis, it can be seen that water is structured in layers from the center of the NT. For this reason, water diffusion was analyzed separately for each water layer from the density profiles: with L_1 and L_2 in the NT interior, and L_3 – L_5 corresponding to successive layers at the outer wall. The difficulty for this kind of calculation is that the layers do not have physical barriers (except between layers L_2 and L_3 , since there is the NT wall), and therefore the water molecules are exchanged between layers. For example, if we follow those water molecules that are in each layer at an initial time, we will observe that in just 100 ps of the MD simulation, depending on the mobility in each layer, most of the molecules will have moved from the initial layer. Consequently, calculating diffusion coefficients in each layer in times of tens or hundreds of nanoseconds becomes impossible using traditional methods such as mean square displacement since the initial molecules do not remain in each layer throughout the simulation. Thus, we calculate the diffusion of water by applying virtual boundary conditions following Liu et al. (2004). This method has been used in studies of transport properties of liquids near a solid interface at the nanoscale

(Rotenberg et al., 2007; Marry et al., 2008; Harder et al., 2009; Greathouse et al., 2015; Lahrar et al., 2019), and it is described in detail by Greathouse et al. (2015).

Calculated diffusion coefficients of water in each layer are shown in Fig. 5. The error bars are calculated as two times the standard deviation for five independent simulations. Uncertainties in computed diffusion coefficients are all reasonably small except for the $N = 9$ pore, which has fewer water molecules. Within each layer, diffusion coefficients were calculated separately for translation perpendicular and parallel to the walls. At both walls, diffusion is hindered (as expected), and mobility increases away from the walls. This is consistent with previous simulations of aqueous solution diffusion in mineral nanopores (Botan et al., 2011; Martins et al., 2014; Greathouse et al., 2015). Diffusion coefficients at the inner walls are nearly zero for all NT models except for $N = 9$, and the planar model. For $N = 9$, water molecules adsorbed to the inner wall have diffusion paths along the wall and parallel to the pore (i.e. $D_{\parallel} \approx D_{\perp}$). This unique feature is discussed in more detail below. Consequently, water diffusion coefficients in the L_2 layer are nonzero and particularly large in the parallel direction. The H-bond environment is different for these L_2 waters in the $N = 9$ NT, which results in more interaction with L_1 waters and a nonzero O density between the L_1 and L_2 layers (Fig. 4). Water transport in this small pore is similar to single file transport in protein channels (Berezhkovskii and Hummer, 2002; Belorizky et al., 2010; Horner and Pohl, 2018), suggesting the possibility for unique separation applications. In the central region of the pore (L_1), water mobility in both directions increases with pore diameter.

Trends in water transport behavior are illustrated in Fig. 6. For all three examples shown in Fig. 6a, b) the longitudinal (z) diffusion occurs almost exclusively for water molecules in the central region. The $N = 12$ trajectories highlight a special situation common for both, $N = 11$ and $N = 12$, with well-defined regions of high water density in the central region and along the wall. This unique feature is confirmed by the radial density profiles for $N = 11$ and $N = 12$ (Fig. 4), which show an exclusion zone between the center and inner-wall regions. Water molecules adsorbed to the $N = 11$ and $N = 12$ interior walls have little probability of jumping to the central region, resulting in an unusually high average water density inside the pores. $N = 9$ is the only case in which longitudinal diffusion is observed in the L_1 layer. In Fig. 6c, diffusion in the inner pore, i.e., considering L_1 and L_2 combined, is shown as a function of N . We found a minimum in the diffusion coefficient as the NT diameter was varied. Importantly, atomistic simulation works commonly report a minimum in energy in vacuum for the similar N values ($N = 10$ – 12), and relate this behavior with the monodispersity found in experiments. Whether there is a link between water diffusion with imogolite diameter control is still an object of discussion. However, to control imogolite diameter, Yucelen et al. (2012b) and Arancibia-Miranda et al. (2017) changed the imogolite precursor, and the solvent composition in the process. In other words, if the solvent diffusion properties influence the imogolite final diameter—a question that remains open—this fact could be used as an alternative route to achieve better control during imogolite synthesis. In this context solvent diffusion predicted from MD could be used as a valuable tool to shed light on this matter.

4. Conclusions

We have studied water dynamics in imogolite using MD simulation. We used the new ClayFF-MOH classical potential, which improves ClayFF by adding angular harmonic terms for a proper description of the Al-O-H and Si-O-H angles. We have considered several nanotube diameters, ranging from $N = 8$ to $N = 15$ repetitions, as well as the planar case ($N \rightarrow \infty$). For $N = 8$, it was found in GCMC calculations that the pore is too small to accommodate water molecules, so the structure and dynamics of water were studied for $N \geq 9$.

Inside the imogolite pore we found a coaxial arrangement of water

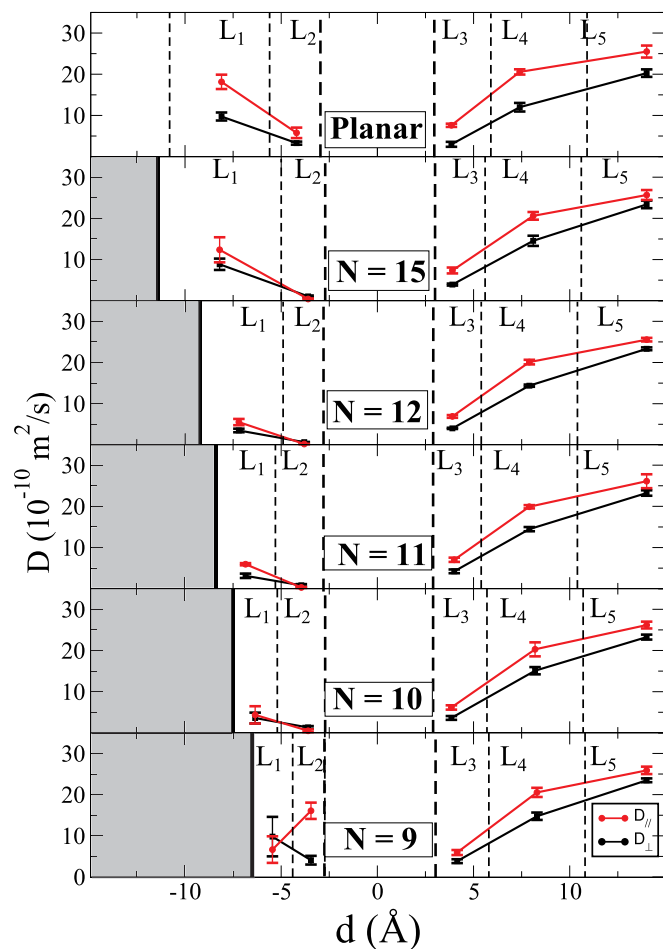


Fig. 5. Axial (D_{\parallel}) and perpendicular (D_{\perp}) diffusion coefficients of water in imogolite. $N = 9, 10, 11, 12, 15$ and planar imogolite. The middle of the NT is marked by a thick black line. The imogolite's wall is denoted by a pair of long dashed lines around $d = 0$.

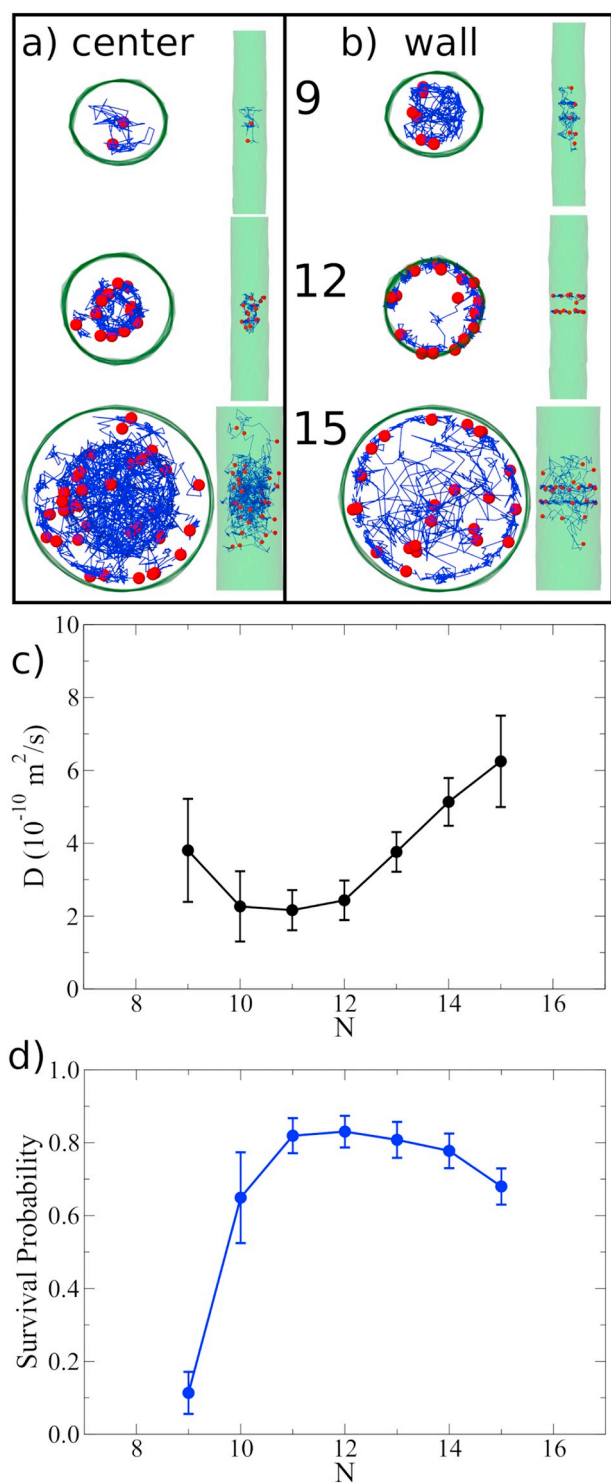


Fig. 6. Trajectories of water molecules during a 0.5 ns time window for $N = 9$, 12, and 15. Top and lateral snapshots of water molecules initially located (a) within 1 nm of the NT symmetry axis and (b) near the inner wall of imogolite. For the sake of simplicity, only the original position of oxygen atoms are shown (red balls). The imogolite surface is colored light green. c) Water diffusion coefficients in the imogolite pores (L1 and L2 layers combined). d) Survival probability of water in the L_1 layer during 30 ps. (For interpretation of the references to colour in this figure legend, the reader is referred to the web version of this article.)

molecules, consisting of a layer of immobile water at the imogolite inner wall, and an inner region with higher water mobility (diffusion) parallel to the nanotube axis. This effect is dependent on the system's

curvature, being more prominent for $N = 10 - 13$.

The mechanism behind the slow diffusion of water molecules closest to the imogolite' inner wall is the formation of H-bonds, evidenced by density profiles of H and O atoms.

At the outer imogolite wall the tendency for H-bond formation is much lower. Nevertheless, an ordered layer of water is formed, accompanied by an increase in water density. Beyond ~ 1.0 nm from the outer imogolite wall, water exhibits bulk-like behavior.

Acknowledgments

This work was supported by the US Department of Energy, Office of Science, Office of Basic Energy Sciences, Chemical Sciences, Geosciences and Biosciences Division. Sandia National Laboratories is a multimission laboratory managed and operated by National Technology and Engineering Solutions of Sandia, LLC., a wholly owned subsidiary of Honeywell International, Inc., for the U.S. Department of Energy's National Nuclear Security Administration under contract DE-NA-0003525. The views expressed in this article do not necessarily represent the views of the U.S. Department of Energy or the United States Government. This work was supported by the *Fondo Nacional de Investigaciones Científicas y Tecnológicas* (FONDECYT, Chile) under grants #1190662, #1160639, #11180557, #1191353, #1190484, AFOSR Grant FA9550-16-1-0122, and *Financiamiento Basal para Centros Científicos y Tecnológicos de Excelencia* CEDENNA AFB180001, and Conicyt PIA/Anillo ACT192023. JRN and SEB acknowledge the support of DICYT project 041931BR and USA1799 Vrdei 041931SB_GO. This research was partially supported by the supercomputing infrastructure of the NLHPC (ECM-02).

Declaration of Competing Interest

The authors declare that they have no known competing financial interests or personal relationships that could have appeared to influence the work reported in this paper.

Appendix A. Supplementary data

Supplementary data to this article can be found online at <https://doi.org/10.1016/j.clay.2020.105582>.

References

- Yucelen, G.I., 2012. Formation and Growth Mechanisms of Single-Walled Metal Oxide Nanotubes. Ph.D. thesis. School of Materials Science and Engineering. <http://hdl.handle.net/1853/44796>.
- Alvarez-Ramírez, F., 2007. Ab initio simulation of the structural and electronic properties of aluminosilicate and aluminogermanate nanotubes with imogolite-like structure. *Phys. Rev. B* 76, 125421.
- Arancibia-Miranda, N., Escudey, M., Pizarro, C., Denardin, J.C., García-González, M.T., Fabris, J.D., Charlet, L., 2014. Preparation and characterization of a single-walled aluminosilicate nanotube-iron oxide composite: its applications to removal of aqueous arsenate. *Mater. Res. Bull.* 51, 145–152.
- Arancibia-Miranda, N., Silva-Yumi, J., Escudey, M., 2015. Effect of cations in the background electrolyte on the adsorption kinetics of copper and cadmium and the isoelectric point of imogolite. *J. Hazard. Mater.* 299, 675–684.
- Arancibia-Miranda, N., Escudey, M., Ramirez, R., González, R.I., van Duin, A.C., Kiwi, M., 2017. Advancements in the synthesis of building block materials: experimental evidence and modeled interpretations of the effect of Na and K on imogolite synthesis. *J. Phys. Chem. C* 121, 12658–12668.
- Barret, S., Budd, P., Price, C., 1991. The synthesis and characterization of imogolite. *Eur. Polym. J.* 27, 609.
- Belorizky, E., Fries, P.H., Guillermo, A., Poncelet, O., 2010. Almost ideal 1D water diffusion in imogolite nanotubes evidenced by nmr relaxometry. *ChemPhysChem* 11, 2021–2026.
- Berendsen, H.J., Postma, J.P., van Gunsteren, W.F., Hermans, J., 1981. Interaction models for water in relation to protein hydration. In: *Intermolecular Forces*. Springer, pp. 331–342.
- Berendsen, H., Grigera, J., Straatsma, T., 1987. The missing term in effective pair potentials. *J. Phys. Chem.* 91, 6269–6271.
- Berezhkovskii, A., Hummer, G., 2002. Single-file transport of water molecules through a carbon nanotube. *Phys. Rev. Lett.* 89, 064503.
- Besoain, E., 1969. Imogolite in volcanic soils of Chile. *Geoderma* 2, 151.
- Besoain, E., Peralta, M., Massaro, S., 2000. Mineralogía y genesis de algunos suelos de

- cenizas volcánicas de Chiloé continental. *Agr. Téc.* 60, 127.
- Botan, A., Rotenberg, B., Marry, V., Turq, P., Noetinger, B., 2011. Hydrodynamics in clay nanopores. *J. Phys. Chem. C* 115, 16109–16115.
- Bottero, I., Bonelli, B., Ashbrook, S.E., Wright, P.A., Zhou, W., Tagliabue, M., Armandi, M., Garrone, E., 2011. Synthesis and characterization of hybrid organic/inorganic nanotubes of the imogolite type and their behaviour towards methane adsorption. *Phys. Chem. Chem. Phys.* 13, 744.
- Brown, W.M., Wang, P., Plimpton, S.J., Tharrington, A.N., 2011. Implementing molecular dynamics on hybrid high performance computers—short range forces. *Comput. Phys. Commun.* 182, 898–911.
- Bursill, L.A., Peng, J.L., Bourgeois, L.N., 2000. Imogolite: an aluminosilicate nanotube material. *Phil. Mag. A* 80, 105.
- Cradwick, P.D.G., Farmer, V.C., Russell, J.D., Masson, C.R., Wada, K., Yoshinaga, N., 1972. Imogolite, a hydrated aluminium silicate of tubular structure. *Nature Phys. Sci.* 240, 187.
- Creton, B., Bougeard, D., Smirnov, K.S., Guilment, J., Poncelet, O., 2008a. Molecular dynamics study of hydrated imogolite. 1. Vibrational dynamics of the nanotube. *J. Phys. Chem. C* 112, 100013.
- Creton, B., Bougeard, D., Smirnov, K.S., Guilment, J., Poncelet, O., 2008b. Molecular dynamics study of hydrated imogolite 2. Structure and dynamics of confined water. *Phys. Chem. Chem. Phys.* 10, 4879–4888.
- Csonka, G.I., Perdew, J.P., Ruzsinszky, A., Phillips, P.H., Lebègue, S., Paier, J., Vydrov, O.A., Ángyán, J.G., 2009. Assessing the performance of recent density functionals for bulk solids. *Phys. Rev. B* 79, 155107.
- Cygan, R.T., Liang, J.J., Kalinichev, A.G., 2004. Molecular models of hydroxide, oxyhydroxide, and clay phases and the development of a general force field. *J. Phys. Chem. B* 108, 1255.
- Davidson, E.R., Feller, D., 1986. Basis set selection for molecular calculations. *Chem. Rev.* 86, 681–696.
- Denaix, L., Lamy, Y., Bottero, J.Y., 1999. Structure and affinity towards Cd^{2+} , Cu^{2+} , Pb^{2+} of synthetic colloidal amorphous aluminosilicates and their precursors. *Colloids Surf. A Physicochem. Eng. Asp.* 158, 315.
- Farmer, V.C., Fraser, A.R., Tait, J.M., 1977. Synthesis of imogolite: a tubular aluminium silicate polymer. *J. Chem. Soc. Chem. Commun.* 462.
- Geraldo, D., Arancibia-Miranda, N., Villagra, N., Mora, G., Arratia-Perez, R., 2012. Synthesis of CdTe QDs/single-walled aluminosilicate nanotubes hybrid compound and their antimicrobial activity on bacteria. *J. Nanopart. Res.* 14, 1286.
- González, R.I., Ramírez, R., Rogan, J., Valdivia, J.A., Munoz, F., Valencia, F., Ramírez, M., Kiwi, M., 2014. Model for self-rolling of an aluminosilicate sheet into a single-walled imogolite nanotube. *J. Phys. Chem. C* 118, 28227.
- González, R.I., Rogan, J., Bringa, E.M., Valdivia, J.A., 2016. Mechanical response of aluminosilicate nanotubes under compression. *J. Phys. Chem. C* 120, 14428–14434.
- González, R.I., Valencia, F.J., Rogan, J., Valdivia, J.A., Sofo, J., Kiwi, M., Munoz, F., 2018. Bending energy of 2D materials: graphene, MoS_2 and imogolite. *RSC Adv.* 8, 4577–4583.
- Greathouse, J.A., Durkin, J.S., Larentzos, J.P., Cygan, R.T., 2009. Implementation of a morse potential to model hydroxyl behavior in phyllosilicates. *J. Chem. Phys.* 130, 134713.
- Greathouse, J.A., Hart, D.B., Bowers, G.M., Kirkpatrick, R.J., Cygan, R.T., 2015. Molecular simulation of structure and diffusion at smectite–water interfaces: using expanded clay interlayers as model nanopores. *J. Phys. Chem. C* 119, 17126–17136.
- Guimarães, L., Enyashin, A.N., Frenzel, J., Heine, T., Duarte, H.A., Seifert, G., 2007. Imogolite nanotubes: stability, electronic, and mechanical properties. *ACS Nano* 1, 362.
- Gustafsson, J.P., 2001. The surface chemistry of imogolite. *Clay Clay Miner.* 49, 73.
- Harder, E., Walters, D.E., Bodnar, Y.D., Faibish, R.S., Roux, B., 2009. Molecular dynamics study of a polymeric reverse osmosis membrane. *J. Phys. Chem. B* 113, 10177–10182.
- Hockney, R., Eastwood, J., 1988. Particle-Particle-Particle-Mesh (P^3M) Algorithms. CRC Press.
- Horner, A., Pohl, P., 2018. Single-file transport of water through membrane channels. *Faraday Discuss.* 209, 9–33.
- Imamura, S., Hayashi, Y., Kajiwara, K., Hoshino, H., Kaito, C., 1993. Imogolite: a possible new type of shape-selective catalyst. *Ind. Eng. Chem. Res.* 32, 600.
- Imamura, S., Kokubu, T., Yamashita, T., Okamoto, Y., Kajiwara, K., Kanai, H., 1996. Shape-selective copper-loaded imogolite catalyst. *J. Catal.* 160, 137.
- Kang, D., Zang, J., Jones, C., Nair, S., 2011. Single-walled aluminosilicate nanotubes with organic-modified interiors. *J. Phys. Chem. C* 115, 7676.
- Kang, D., Tong, H., Zang, J., Jones, C., Nair, S., 2012. Single-walled aluminosilicate nanotube/poly(vinyl alcohol) nanocomposite membranes. *ACS Appl. Mater. Interfaces* 4, 965–976. <https://doi.org/10.1021/am201614w#>.
- Kang, D.Y., Brunelli, N.A., Yucelen, G.I., Venkatasubramanian, A., Leisen, J., Hesketh, P.J., Jones, C.W., Nair, S., 2014. Direct synthesis of single-walled aminoaluminosilicate nanotubes with enhanced molecular adsorption selectivity. *Nat. Commun.* 5, 3342–3351.
- Konduri, S., Mukherjee, S., Nair, S., 2006. Strain energy minimum and vibrational properties of single-walled aluminosilicate nanotubes. *Phys. Rev. B* 74, 33401.
- Konduri, S., Mukherjee, S., Nair, S., 2007. Controlling nanotube dimensions: correlation between composition, diameter, and internal energy of single-walled mixed oxide nanotubes. *ACS Nano* 1, 393.
- Konduri, S., Tong, H.M., Chempath, S., Nair, S., 2008. Water in single-walled aluminosilicate nanotubes: diffusion and adsorption properties. *J. Phys. Chem. C* 112, 15367.
- Kuc, A., Heine, T., 2009. Shielding nanowires and nanotubes with imogolite: a route to nanocables. *Adv. Mater.* 21, 4353.
- Lahrar, E.H., Belhboub, A., Simon, P., Merlet, C., 2019. Ionic liquids under confinement: from systematic variations of the ion and pore sizes toward an understanding of the structure and dynamics in complex porous carbons. *ACS Appl. Mater. Interfaces* 12, 1789–1798.
- Levard, C., Masion, A., Rose, J., Doelsch, E., Borschneck, D., Dominici, C., Ziarelli, F., Bottero, J.Y., 2009. Synthesis of imogolite fibers from decimolar concentration at low temperature and ambient pressure: a promising route for inexpensive nanotubes. *J. Am. Chem. Soc.* 131, 17080.
- Liou, K.H., Kang, D.Y., Lin, L.C., 2017. Investigating the potential of single-walled aluminosilicate nanotubes in water desalination. *ChemPhysChem* 18, 179–183.
- Lisuzzo, L., Cavallaro, G., Lazzara, G., Milioto, S., Parisi, F., Stetsyshyn, Y., 2018. Stability of halloysite, imogolite, and boron nitride nanotubes in solvent media. *Appl. Sci.* 8, 1068.
- Liu, P., Harder, E., Berne, B., 2004. On the calculation of diffusion coefficients in confined fluids and interfaces with an application to the liquid–vapor interface of water. *J. Phys. Chem. B* 108, 6595–6602.
- Liz-Marzan, L., Philipe, A., 1994. Synthesis of platinum nanoparticles in aqueous host dispersions of inorganic (imogolite) rods. *Colloids Surf. A Physicochem. Eng. Asp.* 90, 95.
- Ma, W., Yah, W., Otsuka, H., Takahara, A., 2012. Application of imogolite clay nanotubes in organic–inorganic nanohybrid materials. *J. Mater. Chem.* 22, 11887.
- Marry, V., Rotenberg, B., Turq, P., 2008. Structure and dynamics of water at a clay surface from molecular dynamics simulation. *Phys. Chem. Chem. Phys.* 10, 4802–4813.
- Martin, M.G., 2013. MCCCS Towhee: A tool for Monte Carlo molecular simulation. *Mol. Simul.* 39, 1212–1222.
- Martins, D.M., Molinari, M., Gonçalves, M.A., Mirão, J.P., Parker, S.C., 2014. Toward modeling clay mineral nanoparticles: the edge surfaces of pyrophyllite and their interaction with water. *J. Phys. Chem. C* 118, 27308–27317.
- Mukherjee, S., Bartlow, V.M., Nair, S., 2005. Phenomenology of the growth of single-walled aluminosilicate and aluminogermanate nanotubes of precise dimensions. *Chem. Mater.* 17, 4900.
- Park, S., Yunha, L., Kim, B., Lee, J., Jeong, Y., Noh, J., Takahara, A., Sohn, D., 2007. Two-dimensional alignment of imogolite on a solid surface. *Chem. Commun.* 28, 2917.
- Plimpton, S.J., 1995. Fast parallel algorithms for short-range molecular dynamics. *J. Comput. Phys.* 117 (1), 1–19. <https://www.sciencedirect.com/science/article/pii/S002199918571039X>.
- Pouvreau, M., Greathouse, J.A., Cygan, R.T., Kalinichev, A.G., 2017. Structure of hydrated gibbsite and brucite edge surfaces: DFT results and further development of the classical force field with metal–O–H angle bending terms. *J. Phys. Chem. C* 121, 14757–14771.
- Raabe, G., Sadus, R.J., 2012. Molecular dynamics simulation of the effect of bond flexibility on the transport properties of water. *J. Chem. Phys.* 137, 104512.
- Ramírez, M., González, R.I., Munoz, F., Valdivia, J.A., Rogan, J., Kiwi, M., 2015. Coaxial nanocable composed by imogolite and carbon nanotubes. *AIP Conf. Proc.* 1702, 050005.
- Rotenberg, B., Marry, V., Vuilleumier, R., Malikova, N., Simon, C., Turq, P., 2007. Water and ions in clays: unraveling the interlayer/micropore exchange using molecular dynamics. *Geochim. Cosmochim. Acta* 71, 5089–5101.
- Scalfi, L., Fraux, G., Boutin, A., Coudert, F.X., 2018. Structure and dynamics of water confined in imogolite nanotubes. *Langmuir* 34, 6748–6756.
- Smart, O.S., Neduvetil, J.G., Wang, X., Wallace, B., Sansom, M.S., 1996. Hole: a program for the analysis of the pore dimensions of ion channel structural models. *J. Mol. Graph.* 14, 354–360.
- Stukowski, A., 2010. Visualization and analysis of atomistic simulation data with OVITO—the open visualization tool. *Model. Simul. Mater. Sc.* 18, 015012.
- Teich-McGoldrick, S.L., Greathouse, J.A., Jové-Colón, C.F., Cygan, R.T., 2015. Swelling properties of montmorillonite and beidellite clay minerals from molecular simulation: comparison of temperature, interlayer cation, and charge location effects. *J. Phys. Chem. C* 119, 20880–20891.
- Thomas, B., Coradin, T., Laurent, G., Valentin, R., Mouloungui, Z., Babonneau, F., Baccile, N., 2012. Biosurfactant-mediated one-step synthesis of hydrophobic functional imogolite nanotubes. *RSC Adv.* 2, 426.
- Tuckerman, M., Berne, B.J., Martyna, G.J., 1992. Reversible multiple time scale molecular dynamics. *J. Chem. Phys.* 97, 1990–2001.
- Veerabadrán, N., Price, R., Lvov, Y., 2007. Clay nanotubes for encapsulation and sustained release of drugs. *Nano* 2, 115.
- Wilson, M.A., Lee, G.S.H., Taylor, R.C., 2002. Benzene displacement on imogolite. *Clay Clay Miner.* 50, 348.
- Wu, Y., Tepper, H.L., Voth, G.A., 2006. Flexible simple point-charge water model with improved liquid-state properties. *J. Chem. Phys.* 124, 024503.
- Yah, W., Irie, A., Jiravanichanun, N., Otsuka, H., Takahara, A., 2011. Molecular aggregation state and electrical properties of terthiophenes/imogolite nanohybrids. *Bull. Chem. Soc. Jpn.* 84, 893.
- Yamamoto, K., Otsuka, H., Takahara, A., 2007. Preparation of novel polymer hybrids from imogolite nanofiber. *Polym. J.* 39, 1.
- Yoshinaga, N., Aomine, A., 1962. Imogolite in some ando soils. *Soil Sci. Plant Nutr.* 8, 22.
- Yucelen, G.I., Choudhury, R.P., Vyalikh, A., Scheler, U., Beckham, H.W., Nair, S., 2011. Formation of single-walled aluminosilicate nanotubes from molecular precursors and curved nanoscale intermediates. *J. Am. Chem. Soc.* 133, 5397.
- Yucelen, G.I., Choudhury, R.P., Leisen, J., Nair, S., Beckham, H.W., 2012a. Defect structures in aluminosilicate single-walled nanotubes: a solid-state nuclear magnetic resonance investigation. *J. Phys. Chem. C* 116, 17149.
- Yucelen, G.I., Kang, D., Guerrero-Ferreira, R., Wright, E., Beckham, H.W., Nair, S., 2012b. Shaping single-walled metal oxide nanotubes from precursors of controlled curvature. *Nano Lett.* 12, 827.
- Yucelen, G.I., Kang, D., Schmidt-Krey, I., Beckham, H.W., 2013. A generalized kinetic model for the formation and growth of single-walled metal oxide nanotubes. *Chem. Eng. Sci.* 90, 200.
- Zang, J., Konduri, S., Nair, S., Sholl, D., 2009. Self-diffusion of water and simple alcohols in single-walled aluminosilicate nanotubes. *ACS Nano* 3, 1548.
- Zang, J., Chempath, S., Konduri, S., Nair, S., Sholl, D.S., 2010. Flexibility of ordered surface hydroxyls influences the adsorption of molecules in single-walled aluminosilicate nanotubes. *J. Phys. Chem. Lett.* 1, 1235.
- Zanzoterra, C., Armandi, M., Esposito, S., Garrone, E., Bonelli, B., 2012. CO_2 adsorption on aluminosilicate single-walled nanotubes of imogolite type. *J. Phys. Chem. C* 116, 20417.